Graduate School of Oceanography Faculty Publications

2015

The Gas Transfer through Polar Sea Ice Experiment: Insights into the Rates and Pathways that Determine Geochemical Fluxes

A. Lovely

Brice Loose
University of Rhode Island, bloose@uri.edu

P. Schlosser

W. McGillis

C. Zappa

See next page for additional authors

Citation/Publisher Attribution

The Gas Transfer through Polar Sea Ice Experiment: Insights into the Rates and Pathways that Determine Geochemical Fluxes

Authors

A. Lovely, Brice Loose, P. Schlosser, W. McGillis, C. Zappa, D. Perovich, S. Brown, T. Morell, D. Hsueh, and R. Friedrich

AGU PUBLICATIONS

Journal of Geophysical Research: Oceans

The Gas Transfer through Polar Sea ice experiment: Insights into the rates and pathways that determine geochemical fluxes

A. Lovely[1], B. Loose[1], P. Schlosser[2,3,4], W. McGillis[3,4], C. Zappa[2,4], D. Perovich[5], S. Brown[4], T. Morell[4], D. Hsueh[4], and R. Friedrich[6]

[1]Graduate School of Oceanography, University of Rhode Island, Narragansett, Rhode Island, USA, [2]Department of Earth and Environmental Sciences, Columbia University, Palisades, New York, USA, [3]Department of Earth and Environmental Engineering, Columbia University, New York, New York, USA, [4]Lamont-Doherty Earth Observatory of Columbia University, Palisades, New York, USA, [5]US Army Corps of Engineers Cold Regions Research and Engineering Laboratory, Hanover, New Hampshire, USA, [6]Institute of Environmental Physics, University of Heidelberg, Heidelberg, Germany

Abstract Sea ice is a defining feature of the polar marine environment. It is a critical domain for marine biota and it regulates ocean-atmosphere exchange, including the exchange of greenhouse gases such as CO_2 and CH_4. In this study, we determined the rates and pathways that govern gas transport through a mixed sea ice cover. N_2O, SF_6, ^3He, ^4He, and Ne were used as gas tracers of the exchange processes that take place at the ice-water and air-water interfaces in a laboratory sea ice experiment. Observation of the changes in gas concentrations during freezing revealed that He is indeed more soluble in ice than in water; Ne is less soluble in ice, and the larger gases (N_2O and SF_6) are mostly excluded during the freezing process. Model estimates of gas diffusion through ice were calibrated using measurements of bulk gas content in ice cores, yielding gas transfer velocity through ice (k_{ice}) of $\sim 5 \times 10^{-4}$ m d^{-1}. In comparison, the effective air-sea gas transfer velocities (k_{eff}) ranged up to 0.33 m d^{-1} providing further evidence that very little mixed-layer ventilation takes place via gas diffusion through columnar sea ice. However, this ventilation is distinct from air-ice gas fluxes driven by sea ice biogeochemistry. The magnitude of k_{eff} showed a clear increasing trend with wind speed and current velocity beneath the ice, as well as the combination of the two. This result indicates that gas transfer cannot be uniquely predicted by wind speed alone in the presence of sea ice.

1. Introduction

Sea ice production, transport, and melt occur in regions of the surface ocean where upwelling and downwelling of water from the abyssal ocean take place. Our understanding of sea ice processes indicates that ice formation and physical chemistry may play a role in setting the properties of these abyssal water masses [*Rysgaard et al.*, 2007; *Tamura et al.*, 2008], and possibly in the large-scale air-sea exchange of climatic gases such as CO_2 [*Stephens and Keeling*, 2000; *Hain et al.*, 2010]. In addition to its impact on air-sea exchange, sea ice itself may be an important annual sink of CO_2 [*Delille et al.*, 2014]. To quantify the hierarchy of processes that take place in the sea ice zone, we need to understand how sea ice affects gases in the ocean beneath ice, and how sea ice processes can lead to air-sea gas exchange [*Loose et al.*, 2014].

The flux of gas at the air-sea interface can be described as the product of a kinetic rate constant and the concentration differential (ΔC) across the interface: $F = k\Delta C$, where k is the rate constant or gas transfer velocity. The most common approaches to estimating k utilize a quadratic relationship with wind speed [e.g., *Wanninkhof*, 1992] that was determined for the coastal and open ocean with mature wave fields. In sea ice covered regions, this wind speed-derived estimate of k has typically been scaled to the fraction of open water (f) [*Stephens and Keeling*, 2000; *Arrigo and van Dijken*, 2007; *Takahashi et al.*, 2009]. However, this approach, while simple and logical, is not based upon field or model estimates of k in sea ice and there is evidence that it is not a good representation of the real dynamics in these regions. In fact, the relationship between wind speed and turbulence may diminish as fetch is reduced while other processes such as current shear between the water and ice may dominate [*McPhee*, 1992]. Sea ice can be permeable to gases [*Gosink et al.*, 1976; *Golden*, 2001] so that ventilation from sea ice covered waters can be a result of transport through the ice (k_{ice}) or open water (k). Sea ice cover has spatial structure (e.g., floes, leads, and ridges) down to the scale of meters, yet most of the available sea ice data products can only resolve ice cover on

the scale of tens of kilometers. Consequently, it is necessary to work with a homogenized version of the gas transfer velocity where we resolve the bulk rate of transfer averaged over a given spatial scale [*Loose et al.*, 2014],

$$k_{eff} = (1-f)k_{ice} + (f)k \qquad (1)$$

Here $(1 - f)$ is the fraction of sea ice covered water and k_{eff} represents the effective gas transfer velocity. Methods using tracers to determine ocean/atmosphere gas fluxes, such as the radon deficit method [*Rutgers Van Der Loeff et al.*, 2014], the dual tracer method [*Ho et al.*, 2011], or tracer mass balance (used here) estimate k_{eff} while those using covariance flux or the gradient flux method approximate k or k_{ice} as they average over smaller time and space scales.

Presently, we can build on a small but important collection of estimates of k and k_{eff} from ice-covered regions. The picture that emerges from these data is not entirely coherent. The study by *Fanning and Torres* [1991] has frequently been used as a reference, primarily because it has been the only available estimate of k_{eff} for almost 20 years. The estimates of Fanning and Torres using the ^{222}Rn deficit method in the Barents Sea yielded values of k_{eff} ranging from 1.4 to 6.2 m d^{-1} in greater than 50% ice cover (here we have normalized these values of k_{eff} to a Schmidt number of 600, where the Schmidt number is the ratio of water viscosity to molecular diffusivity). Subsequently, *Loose and Schlosser* [2011] published estimates of k_{eff} using salinity, ^{3}He and CFC-11 budgets from the drifting Ice Station Weddell (January–June 1992). Their estimate yielded an average of k_{eff} of 0.11 m d^{-1} for almost 100% ice cover. This value would seem to indicate that exchange continues to occur in the limiting sea ice condition, suggesting that the ice pack is not completely closed. Recently, *Rutgers van der Loeff et al.* [2014] used the radon deficit method to measure gas transfer velocities at both ice-covered and ice-free stations in the Arctic Ocean. At ice-covered stations, they observed no detectable radon deficit. This study reflects some of the challenges to making gas transfer velocity measurements in ice-covered regions. During the course of that study, cold conditions led to active ice formation during much of the study. Ice formation may also have led to mixed-layer deepening and entrainment of excess radon. Nevertheless, two radon profiles were obtained for ice covers that were approximately 80% and at these stations they observed k_{eff} of 0.1 and 0.56 m d^{-1}, also indicating measurable air-sea exchange. Collectively, the estimates by *Loose and Schlosser* and *Rutgers van der Loeff et al.* [2014] indicate nonnegligible gas exchange takes place above 50% ice cover, but they are much smaller values for k_{eff} than the study by *Fanning and Torres* [1991].

In addition to air-sea exchange, the absorption capacity of the sea ice microstructure for gases has to be understood to close the mass balance. *Gosink et al.* [1976] found that sea ice is permeable to gases at all temperatures, especially above −10°C, and they report diffusivities ranging from $D = 10^{-7}$ to 10^{-5} cm^2 s^{-1}. *Loose et al.* [2011] measured the diffusivity of SF$_6$ and O$_2$ across sea ice in different laboratory conditions. They report higher values for D in the range of 10^{-4} to 10^{-5} cm^2 s^{-1}. This wide range of diffusivities (10^{-7} to 10^{-4} cm^2 s^{-1}) may reflect the complex processes that take place within sea ice, including the large temperature dependence of sea ice porosity [*Golden*, 2001] and bubble processes, which can nucleate as free gas or redissolve within sea ice as temperatures change, advect within brine channels, and rise vertically due to buoyancy [*Moreau et al.*, 2014; *Zhou et al.*, 2013; *Crabeck et al.*, 2014].

Here we will explore the flux of gases across the ice-water interface, as well as within sea ice. We interpret individual estimates of k_{eff} and k_{ice} from dissolved gas budgets, in terms of sea ice and ice-adjacent processes—namely brine drainage and ice melt, but also solute rejection during freezing and the solubility of gas within the ice crystal lattice. Our study was performed in a large-scale laboratory experiment in which the fraction of open water, water current, wind speed, and air-water temperature gradient are controlled. Values for D, the bulk gas diffusivity, are determined using numerical methods, which then allow us to determine k, k_{eff}, and k_{ice}. The experimental setup has been designed to examine ice-water and air-water transfer rates. These results cannot easily be used to make inferences about air-ice fluxes because, unlike natural sea ice, we expect no significant authigenic production/consumption of biogenic gases such as O$_2$, CO$_2$, CH$_4$, or DMS. Therefore, the boundary conditions driving air-ice gas fluxes in natural sea ice are entirely distinct from the conditions in this experimental setup.
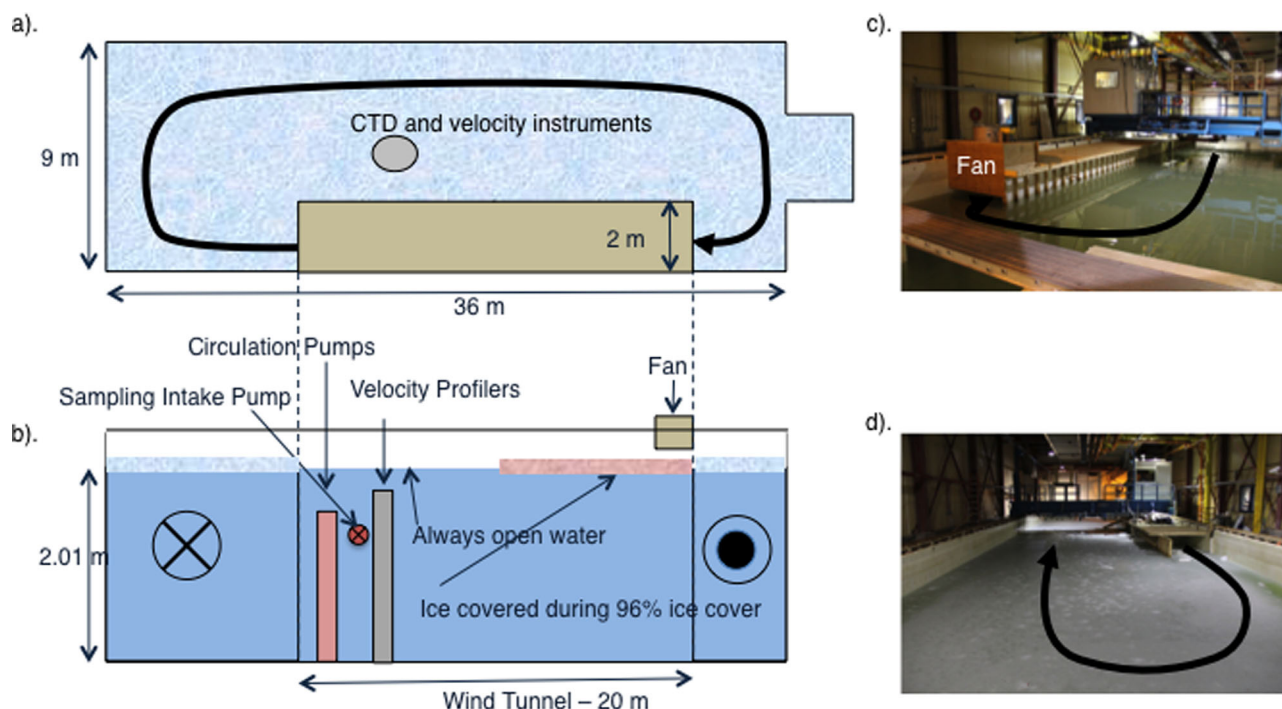
Figure 1. Diagram of the CRREL test basin during the GAPS experiment. (a) A plan view of the test basin. The light blue stippled pattern indicates ice covered throughout the experiment. (b) A section view of the test basin. The pink stippling indicates the increase in ice cover from the long to the short lead experiment. (c) View looking west across the test basin. The black arrows indicate flow direction. (d) View looking east across the test basin. The end of the wind tunnel is seen on the right. Arrow represents the direction of flow of the water beneath the ice.

2. Methods

2.1. Experiment Setup and Analytical Measurements

The GAPS (Gas Transfer through Polar Sea ice) experiment was conducted in the Ice Engineering Test Basin at the US Army Corp of Engineers Cold Regions Research and Engineering Lab (CRREL) at Hanover, NH. This is a $36 \times 9 \times 3$ m pool located in a temperature-controlled room that can reach temperatures as low as $-29°C$. Along one side, a 20×2 m wind tunnel was constructed containing a steel belt-drive ducted fan with a maximum rated flow of 430 m^3 min^{-1} that blew air through a flow straightener and along the water surface through the length of the wind tunnel. Four submersible impeller pumps powered by $1/2$ HP 460 V three-phase motors produced a maximum water flow rate of 7 m^3 min^{-1}. The pumps were placed at the western end of the tunnel to circulate the water through the test basin in the same direction as the wind (Figure 1). The fan and pumps were run on separate variable frequency drives and could be set to run at any frequency between 0 and 60 Hz, which has the effect of modulating their speed.

Measurement of the wind speed inside the tunnel was carried out using Vaisala WS425 and WMT700 anemometers, both of which were suspended over the test basin from the roof of the wind tunnel. The height of the wind tunnel as 76 cm, and wind speed was measured vertically at two or more heights above the water surface by moving one anemometer vertically. The second anemometer remained stationary to measure wind speed always in the same location. The wind speed profile was used to estimate the drag coefficient (C_d), assuming a log linear relationship between wind speed and height above the water surface. Using C_d and the measured wind speed inside the wind tunnel, we subsequently calculated the 10 m wind speed (U_{10}), using the method described by *Mesarchaki et al.* [2014] (Table 1). Three Nortek Aquadopp Profilers, instruments for measuring three-dimensional velocity, were placed in the channel 0.85 m off the bottom (1.05 m below the water surface) looking upward at the water surface, which was intermittently ice covered. Each sampled at 2 Hz for a 20 min period every hour over which the profiles were averaged. Outside the wind tunnel, there is no mechanically induced air circulation within the test basin, so that only the ice surface inside the wind tunnel is being impacted by wind.

A CTD was mounted in the test basin to track salinity and temperature changes within the basin and an array of thermistor sensors was deployed along the outer edge of the wind tunnel ranging from 10 cm

Table 1. Forcing Scenarios Conducted During the GAPS Experiment at CRREL and the Results of Each[a]

Scenario	f	Ice Thickness (cm)	Ice Salinity, S_i (psu)	Pump Speed (Hz)	Fan Speed (Hz)	Water Velocity (m s^{-1})	U_{10} (m s^{-1})	k_{ice} (m d^{-1})	Mean k_{eff} (m d^{-1})
1	0.09	8.5	6.9	60	0	0.145	0.18	8.92E-4	0.26
2	0.09	8.5	6.5	20	0	0.045	0.88	8.92E-4	0.13
3	0.09	8.5	6.5	5	60	0.015	5.69	8.92E-4	0.33
4	0.09	8.5	6.0	5	20	0.017	1.97	8.92E-4	0.00
5	0.04	18.5	6.4	60	0	0.156	4.15	4.93E-4	0.11
6	0.04	19	6.2	5	60	0.0253	6.50	4.93E-4	0.03
7	0.04	17	5.7	40	60	0.120	4.10	4.93E-4	0.31

[a]Long lead experiments are those with an open water fraction of $f = 0.09$, and the short lead experiments are those with $f = 0.04$.

above the target ice surface to 60 cm below this point. The test basin was filled with fresh water and ∼20 metric tons of 98% pure NaCl was mixed with the water to obtain a salinity of close to that of surface water in polar regions. Air was bubbled into the water to help dissolve the salt and the conductivity sensor on the CTD was used to check the salinity against that calculated to make sure all of the salt dissolved. Salt dissolution and brine drainage from the ice during freezing combined to bring the salinity to approximately 27.5 practical salinity unit (psu) when the experiment began (day 2 in Figure 2).

SF_6, N_2O, ^3He, and CO_2 were added to the tank using two approaches, depending on the objectives for the tracer. A timeline of the experimental sequence can be found in Figure 3. CO_2 was used to measure gradient fluxes of gas in the wind tunnel above the water, but not for mass balance calculations as with the other tracers. The gradient flux method requires a very high water concentration of CO_2, which could only be achieve by bubbling with diffusion stones before the surface of the test basin was frozen. Bubbling with CO_2 continued until the concentration reached ∼1.07 mol m^{-3} (15,000 ppmv) (Figure 4). The results of the gradient flux wind tunnel experiments will be reported in a separate contribution. The test basin was then frozen to an ice thickness of 8.5 cm.

After freezing, the remaining gas tracers were added: a total of 8.21 mol N_2O and 2.23×10^{-4} mol SF_6 were diffused into a gas-tight 500 gal. (1.9 m^3) tank and, at the completion of freezing (day 2.5), this water was added to the test basin. On day 3.5, 1.83×10^{-6} mol of ^3He was added (Figure 4). In this way, SF_6, N_2O, and ^3He were added to the test basin without introducing tracer into the ice matrix itself and without producing bubbles that would be trapped beneath the ice. If minimal gas tracer ends up in the ice, it is less complicated to account for exchanges between the ice and the water. During each addition, the water pumps
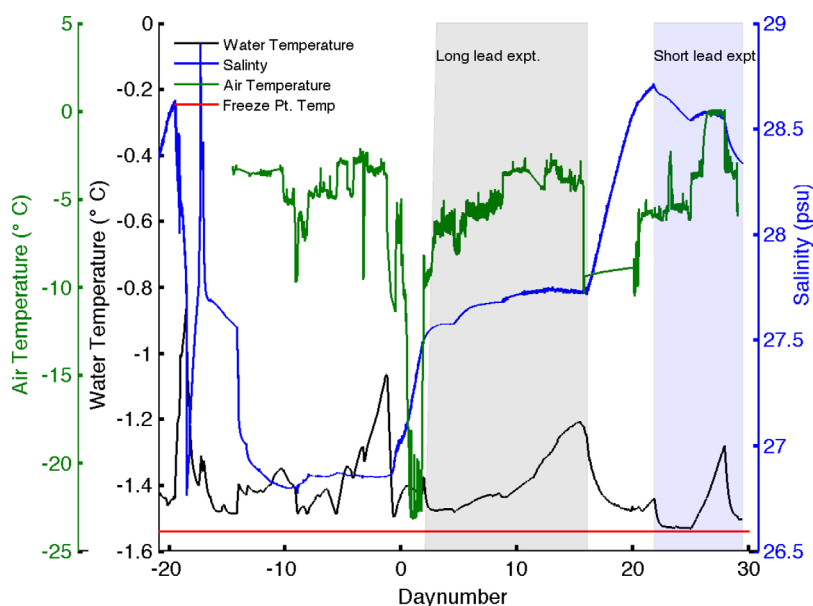

Figure 2. Air and water temperature as well as salinity of the test basin throughout the GAPS experiment. The red line indicates the freezing point temperature at 28.5 psu (−1.54°C). Daynumber = 0 corresponds to the day that the lead experiments began; the negative days numbering corresponds to the ice floe experiments not described in this manuscript.
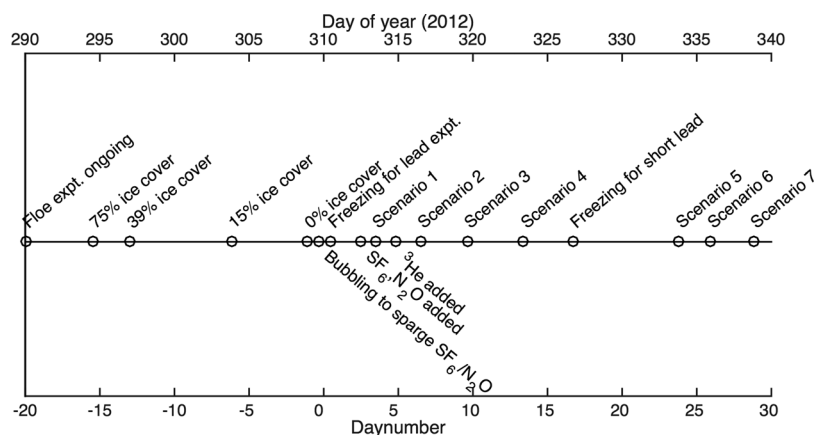
Figure 3. A timeline for the GAPS experiment, showing the daynumber time base, where 0 corresponds to the beginning of the lead experiments, which are the subject of this manuscript. The upper axis depicts the 2012 day of year for each event. The experimental setup in Scenarios 1–7 is detailed in Table 1.

were set to their maximum speed to mix the gases through the entire test basin. When the pumps ran at maximum, the mixing time scale of the tank was much faster than the gas exchange time scale, ensuring that the boundary conditions for gas exchange were horizontally homogeneous. This can be demonstrated by considering that at the vertically averaged flow velocity of 0.15 m s^{-1}, the tank volume (714 m^3) was recycled through the pumps in approximately 20 min. The rapid mixing of the tank can also be observed in the time series of CO_2 addition to the test basin. The unsmoothed pCO_2, sampled every 2 s, shows that as CO_2-rich water from the 500 gal. tank drains into the test basin, it is rapidly mixed to produce a homogeneous concentration (Figure 5). If inhomogeneities existed, variations between the baseline concentration (e.g., 0.07 mol m^{-3}) and the plateau concentration (e.g., 0.18 mol m^{-3}) would have been observed. Instead, the concentration increased monotonically by 157% in less than 3 h.

Multiple scenarios of varying pump and wind speed were run (Table 1). Scenarios 1–4 were performed with a 16 m opening inside the wind tunnel; these are the "long lead scenarios" when ice covered 91% of the test basin surface. A second freezing event began on day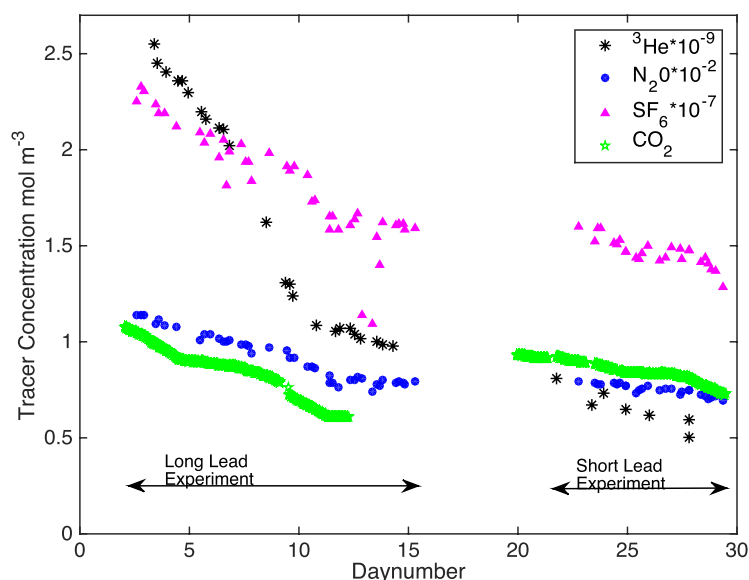 17 to shorten the lead to 5 m, or 96% overall ice cover. Ice thickness increased to 18.5 cm, while salinity increased from 27.75 to 28.7 psu (Figure 2). CO_2 was again bubbled directly into the test basin before freezing, producing an initial concentration of ~1.07 mol m^{-3}. Three additional forcing scenarios were completed. Gas exchange was induced by the production of turbulence from the pumps or fan (Table 1). These are the "short lead scenarios."

2.2. Gas Tracer Sampling and Analysis

To sample test basin water and determine the concentration of each tracer gas throughout the experiment, a 12V Rule-360 submersible

Figure 4. Concentration of the four gas tracers (^{3}He, N_2O, SF_6, and CO_2) in the test basin. The rate of decrease varies depending on the conditions present in the test basin. CO_2 data were not used for mass balance calculations due to uncertainties regarding the carbonate system in the test basin.
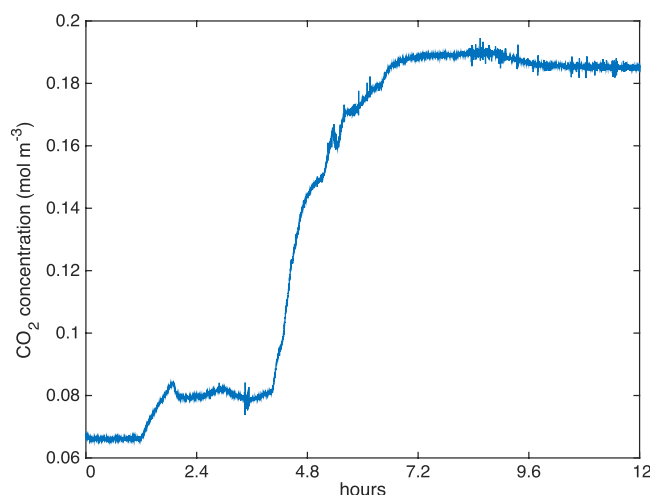
Figure 5. A time series of CO_2 addition to the test basin in preparation for a gas evasion experiment. The pCO_2 is measured every 2 s using a membrane contactor and Licor LI-840. As CO_2-rich water from the 500 gal. tank is gradually added to the test basin, the water is rapidly mixed to produce a homogeneous concentration.

pump was installed in the test basin channel (Figure 1) 145 cm off the bottom (45 cm below the water surface). Vinyl tubing was attached to the pump to create a continuous flow loop that ran from the test basin into the adjacent laboratory and back to the basin. A three-way valve setup in the lab allowed water samples to be collected for N_2O, SF_6, ^3He, and DIC/alkalinity analysis.

To measure N_2O and SF_6, 20 mL water samples were collected in 50 mL ground glass syringes for analysis via the headspace method. Approximately 30 mL of nitrogen was added to each syringe before samples were equilibrated to room temperature and shaken for 10 min to achieve solubility equilibrium [*Wanninkhof et al.*, 1987].

The gaseous samples were injected into an SRI-8610C Gas Chromatograph with an Electron Capture Detector (GC-ECD). The concentrations of tracer in the test basin water (C_w) could then be determined using the equilibrium solubility and ideal gas behavior in the syringe,

$$C_w = X\left(H + \frac{P}{RT}\frac{V_a}{V_w}\right) \qquad (2)$$

where X is the partial gas pressure, determined by multiplying the measured peak area by the predetermined calibration factor, H is Henry's equilibrium solubility constant, P is atmospheric pressure, R is the ideal gas constant, T is temperature, V_a is the volume of gas in the syringe, and V_w is the volume of water in the syringe. Equilibrium solubility and gas saturation state were determined using the empirical gas solubility relationships described in *Bullister et al.* [2002] (SF_6), *Weiss* [1974] (CO_2), *Weiss and Price* [1980] (N_2O), and *Weiss* [1971] (He and Ne).

Samples for ^3He analysis were taken in copper tubes and analyzed at the Lamont-Doherty Earth Observatory of Columbia University on a dedicated VG5400 mass-spectrometer (^3He and ^4He) and a Pfeiffer PrismaPlus quadrupole mass-spectrometer (Ne). The measured concentrations of the tracer gases throughout the experiment are shown in Figures 4 and 6.

Concurrent with the discrete ^3He, SF_6, and N_2O analyses, the continuous flow water loop was analyzed for pCO_2 using a membrane contactor and a LICOR LI-840A CO_2/H_2O analyzer. Water samples were also taken every 4 h to
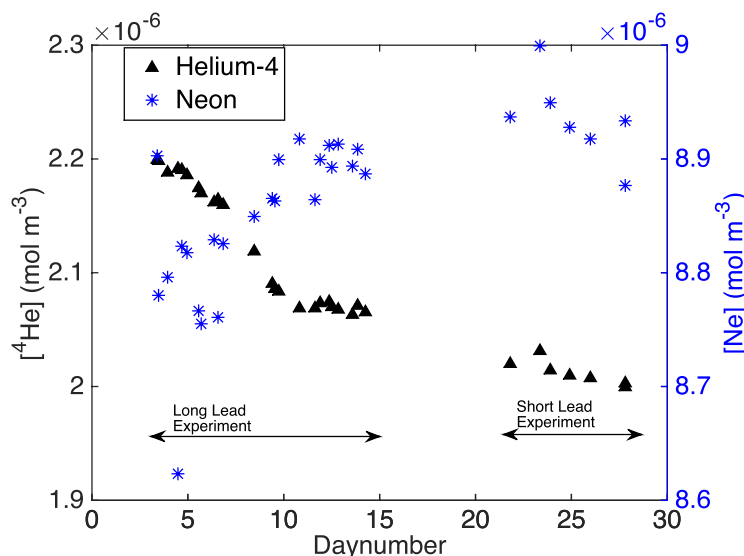

Figure 6. Concentration of ^4He and Ne in the test basin during the experiment. Both gases entered the tank as a result of bubbling the water with air when dissolving the salt. Ne concentration increases as it is rejected from the ice during freezing. ^4He is also rejected from the ice but its concentration decreases as it is also escaping through the air-water interface at a rate much fast than Ne due to its greater supersaturation and smaller size.
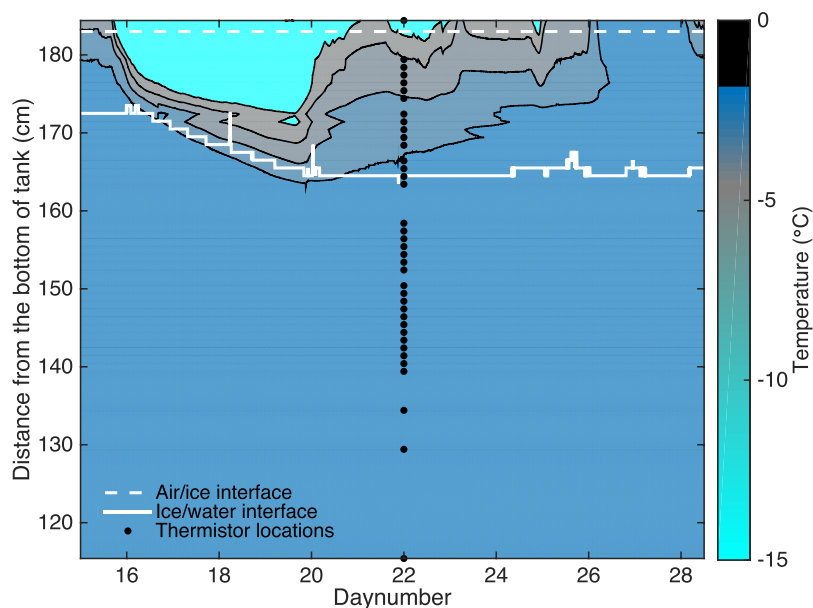
Figure 7. Contour plot of thermistor string temperature that was embedded in the ice. The white dashed line indicates the air/ice interface and the solid white line indicates the ice/water interface as measured by the sonar altimeter. Temperature measurements were taken every 5 min.

monitor DIC and alkalinity in the test basin. Respiration in these samples was inactivated with mercuric chloride and samples were stored in sealed jars for analysis at the University of Rhode Island.

Air samples taken in the cold room were analyzed for SF_6 and N_2O using the GC-ECD and the air-water concentration differentials at equilibrium (C_a) were determined in mol m^{-3} using

$$C_a = XH \tag{3}$$

Two ice cores were collected daily to observe ice thickness, and the accumulation of SF_6 and N_2O in the ice through diffusion. One core was melted in an airtight container with a pure N_2 atmosphere for later headspace analysis [*Loose et al.*, 2009]. Cores were 7.6 cm in diameter, and total ice volume for gas analysis ranged between 122 and 275 mL. Once the core was melted, the container was shaken to achieve solubility equilibrium and analyzed with the GC-ECD using the headspace method [*Wanninkhof et al.*, 1987]. Ice thickness and water depth were monitored using an upward-looking Benthos PSA-916 sonar altimeter mounted on the bottom of the test basin. A second core was taken each day for ice crystal structure analysis, which was carried out on-site at CRREL.

A thermistor string collected temperature data at 1 cm (5 cm at the very top and bottom) intervals along a 65 cm depth range that extended from the air, through the ice into the water (Figure 7). However, the data logger recording ice temperature stopped recording and this was not discovered until day 15, resulting in no ice temperature data from days 0 to 15. A handheld salinometer was also used daily to check the water column for stratification.

2.3. Data Interpretation

The mass balance of an inert gas tracer was used to infer gas flux from the water to the air and to the ice. Over short time intervals (i.e., days), the gas tracer mass balance in the tank was determined by

$$\frac{dM}{dt} = F_{ice} + F_{air} \tag{4}$$

$\frac{dM}{dt}$ is the change in tracer mass in the test basin through time, F_{ice} is the flux of tracer from the water to the ice, and F_{air} is the flux of tracer from the water to the air. This equation states that there are no internal sources or sinks for the gas tracers and the only loss terms are the gas fluxes. F_{ice} was first determined using a numerical solution for gas diffusion and then used to calculate F_{air}:

$$F_{air} = \frac{dM}{dt} - F_{ice} \qquad (5)$$

For the numerical solution, it is necessary to determine the bulk gas diffusion coefficient through the ice; this determination is described in the next section.

2.3.1. Gas Diffusion Coefficient

To estimate the flux of gas into the ice, values for the diffusion coefficient (D) were determined for SF_6 and N_2O using a finite difference solution to the one-dimensional diffusion equation through a porous medium,

$$\frac{\partial C_{ice}}{\partial t} = D \frac{\partial^2 C_{ice}}{\partial z^2} \qquad (6)$$

This approach assumes that the flux of gas can be directly related to the vertical gradient in solute concentration by a single coefficient, D. Here C_{ice} is the bulk concentration of each gas in the ice. Gas was assumed to move through the ice in the vertical direction ($D = D_z$). Horizontal diffusion (D_x) was not included, as the capillary structure of sea ice makes $D_x \ll D_z$ [*Golden*, 2001]. This approach to modeling the gas transport does not attempt to explicitly represent the geometry of the sea ice microstructure, which limits the ability to resolve changes in diffusivity caused by changes in the ice microstructure. However, the resulting bulk diffusivity parameter, D, is equivalent in from to what has been measured in the field [*Gosink et al.*, 1976; *Crabeck et al.*, 2014] and in the laboratory [*Loose et al.*, 2011], so we consider this formulation to be the appropriate level of complexity, given the available data.

The boundary conditions at the ice-water interface were determined from the time series of gas concentration in the water. Likewise, the boundary condition at the air-ice interface was estimated from the measured gas partial pressure in the air above the test basin, which is converted to a gas concentration using the Henry's law solubility relationship. The initial concentration of gas in the ice was zero for the long lead (91% ice cover), as the pool was gas free when ice formed. A second model run was initiated for the short lead (96% ice cover) with the same boundary conditions except the initial gas concentration in the ice was set to the modeled profile concentration at the end of the long lead scenario.

The model was solved iteratively using a range of D values and the bulk concentration of gas in the ice through time was calculated for each D. The D chosen was that whose bulk concentrations had the smallest residual difference between the modeled and the measured bulk concentrations of N_2O and SF_6.

The gas tracer flux from the tank to the ice, F_{ice} at time t was calculated by

$$F_{ice} = A_{ice} * \frac{N*dz}{dt} \sum_{j=1}^{N} \left(C_j^{t+1} - C_j^t \right) \qquad (7)$$

A_{ice} is the surface area of the ice, N the number of nodes through the ice in the finite difference model, dz the thickness of a single node, and C the concentration of tracer in the ice at time t and node j. F_{ice} has units of moles per time. Finally, the mean value of D from all four scenarios was used to estimate k_{ice} by dividing D by z_{ice}—the thickness of the ice, which can also represent the diffusive length scale.

2.3.2. Gas Transfer Velocity k_{eff}

Having determined the moles of gas (M) that were lost to the ice, we can compute a new gas budget for the test basin that has been corrected for the effect of gas diffusion into the ice. This is the budget we want to use in order to estimate the gas transfer velocity. To correct $C_w(t)$, we replace $F_{ice}(t)$ back into the water as

$$M_w(t) = M_{obs}(t) + F_{ice} * dt \qquad (8)$$

where M_w and M_{obs} are the calculated and observed moles of gas in the water. This leads to a corrected value for $C_w^{corr}(t)$ in terms of the calculated moles of gas in the test basin (V),

$$C_w^{corr}(t) = \frac{M_w(t)}{V} \qquad (9)$$

Finally, the corrected value of $C_w(t)$ can be used to calculate k_{eff} [*Loose et al.*, 2014]:
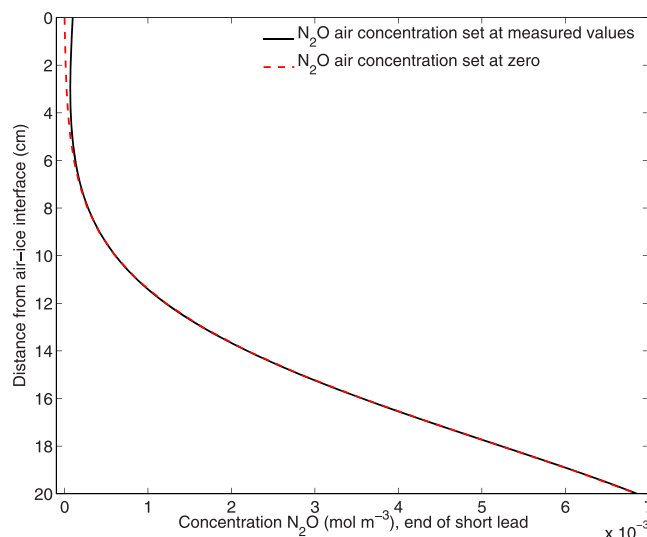
Figure 8. Modeled concentration profile of bulk N_2O concentration in the ice at the end of the experiment (daynumber 30). The two profiles reflect the upper (air) boundary condition: dashed line resulted from using $N_2O = 0$ in the air, and the solid line resulted from the measured time series of N_2O concentration in air. The small difference reflects diffusion from the air into the ice.

$$k_{eff} = \frac{h}{dt} \ln\left(\frac{C_{wi}^{corr} - C_a}{C_{wf}^{corr} - C_a}\right) \quad (10)$$

h is the measured water depth in the pool, dt is the length of the scenario (days), and C_a is the concentration of gas in the air. A best fit line through the measured $C_w(t)$ for each scenario (period of constant forcing conditions where the wind speed and water current did not change) was used to estimate the initial (C_{wi}^{corr}) and final (C_{wf}^{corr}) gas concentrations during each scenario.

Using the flux-gradient version of Fick's law ($F = -D\frac{dc}{dz}$) at the top of the ice, we estimated the gas transport at the air-ice interface and found it to be zero. In other words, gas appeared to diffuse into the ice, but diffusive transport from the water to the air (through 20 cm of ice) was negligible over a period of ∼30 days (Figure 8).

All values of k_{eff} were normalized to k_{600} using the Schmidt number relationship $k_{eff} = k_i\left(\frac{600}{Sc_i}\right)^{-0.5}$.

3. Results

3.1. Evolution of Ice and Salt Properties During GAPS

The salinity in the test basin increased by nearly 1 psu during each ice formation event (day 0–3, days 16–21) when large amounts of brine were rejected from the ice during freezing (Figure 2). By dividing the increase in salinity by the change in ice thickness, it was determined that a 0.1 psu increase in test basin salinity resulted from every centimeter of ice grown. Smaller variations of hundredths to tenths of a psu were evident despite near constant ice thickness. These small increases in salinity can result from a small amount of frazil ice formation on the water surface or an increase in air temperature causing the ice to warm and the brine to drain out [*Petrich and Eicken*, 2009]. Small decreases may result from erosion of the underside of the ice and subsequent melt (days 22–25, days 27.5–29.5). Overall, through most scenarios, salinity remained fairly constant.

Microphotographs of the ice crystal structure using cross-polarizing light filters helps to demonstrate that the ice formed in the test basin had a structure similar to that observed in natural sea ice (Figure 9). Crystals near the ice/air surface (Figure 9b) are smaller than those near the water/ice boundary due to the initial formation of frazil ice that occurs before the columnar dendritic structure takes over [*Petrich and Eicken*, 2009].

The thermistor string frozen into the ice revealed a temperature gradient through the ice ranging from −15°C at the cold air/ice interface to −1.5°C at the ice/water interface (Figure 7). The gradient was greatest when a large air/water temperature difference was present. As expected, the ice is coldest at the surface and warms toward the ice-water interface. This is most distinct during the period of ice formation preceding the short lead scenarios (days 16–20). During the short lead scenarios (days 22–30), the air temperature is continually adjusted around −5 °C to maintain constant ice thickness. Compared to natural sea ice, the ice in these experiments is quite warm. These conditions are conducive to brine drainage from the ice [*Golden et al.*, 1998].

We increased the room temperature at times to discourage frazil ice formation over the lead during scenarios with wind. This resulted in the surface temperature of the ice increasing and, when air temperature warmed (above the freezing temperature on day 26–27), an inverted temperature gradient is evident through the ice; the very surface is warm (−0.8°C) and then gets colder (−1.8°C) near 3 cm below the ice
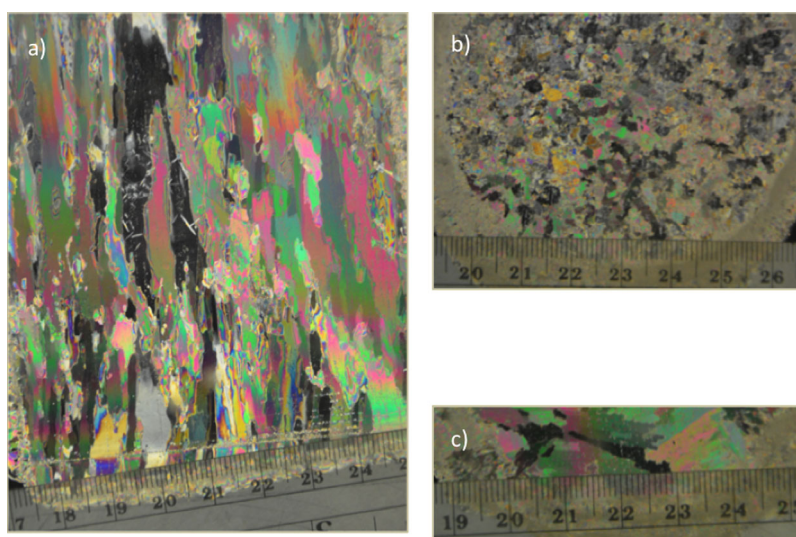
Figure 9. Thin section micrography of the laboratory sea ice in the test basin during the GAPS experiment, seen under cross-polarized light. Individual ice crystals can be distinguished by the change in crystal orientation that leads to a spectral shift in the illumination. (a) Vertical cross section. (b) Horizontal cross section taken at the top of the core showing small crystals near the warm ice-air interface. (c) Horizontal cross section taken at the bottom of the core showing the much larger platelets near the ice-water interface.

surface before warming to the water temperature near $-1.5°C$. Under conditions such as these, the ice can become more permeable with respect to gas diffusion [*Golden*, 2001].

3.2. Carbonate System in the Test Basin

Given the large excess pCO_2, it was reasoned that a DIC budget for the tank might also be possible, if the water in the test basin had low or no alkalinity allowing any change in DIC to be due to changes in the large excess of pCO_2. Unfortunately, the water in the test basin turned out to be of very high alkalinity (3.8–3.9 mM) compared to that of normal seawater ($\sim$2.2 mM). Further analyses determined that the roughly 2% of impurities by volume in the 98% NaCl could have been pure phosphate (5.7 mM in the test basin), hydroxide (32 mM in the test basin), bicarbonate (8.9 mM in the test basin), or a combination of these and other alkaline compounds. Our inability to constrain the carbonate system in the test basin preempted us from treating dissolved CO_2 as a conservative tracer and observe how it compared with the other gas budget calculations.

3.3. Evolution of Gas Properties During GAPS

The concentration of SF_6, N_2O, and ³He decreased monotonically over time in the test basin reflecting gas evasion (Figure 4). The rate of decrease varied depending on the physical forcing conditions that led to turbulence in the basin. When analyzing the ⁴He and Ne samples (Figure 6), we observed an excess above saturation in ⁴He and Ne: ⁴He concentrations initially were in excess of saturation by $\sim$16% but declined to 5% excess by the end of the experiment. In contrast, Ne was initially supersaturated by 2%, and this Ne excess increased to nearly 5% by the end of the lead experiments.

4. Discussion

4.1. Rate of Bulk Diffusion Through the Laboratory Sea Ice

The time series of bulk gas concentration in the sampled ice cores most closely resembled the modeled gas concentration, when D was of the order of 10^{-6} cm^2 s^{-1} (Figure 10). The average value of D from the lead experiments was $5.5 \pm 1.4 \times 10^{-6}$ for SF_6 and $2.7 \pm 0.3 \times 10^{-6}$ cm^2 s^{-1} for N_2O (Table 2). The ratio of these two diffusivities does not follow the Graham's law relationship, which predicts faster diffusivity for gases with lower molecular weight. A similar result was observed by *Loose et al.* [2011] who measured diffusion of O_2 and SF_6, also in laboratory experiments, and found that the diffusion coefficient of SF_6 (the heavier gas) was greater than that for O_2. *Loose et al.* argue that solubility can be more important than gas kinetics in determining the gas diffusion through sea ice. Their model analysis of the laboratory data showed that
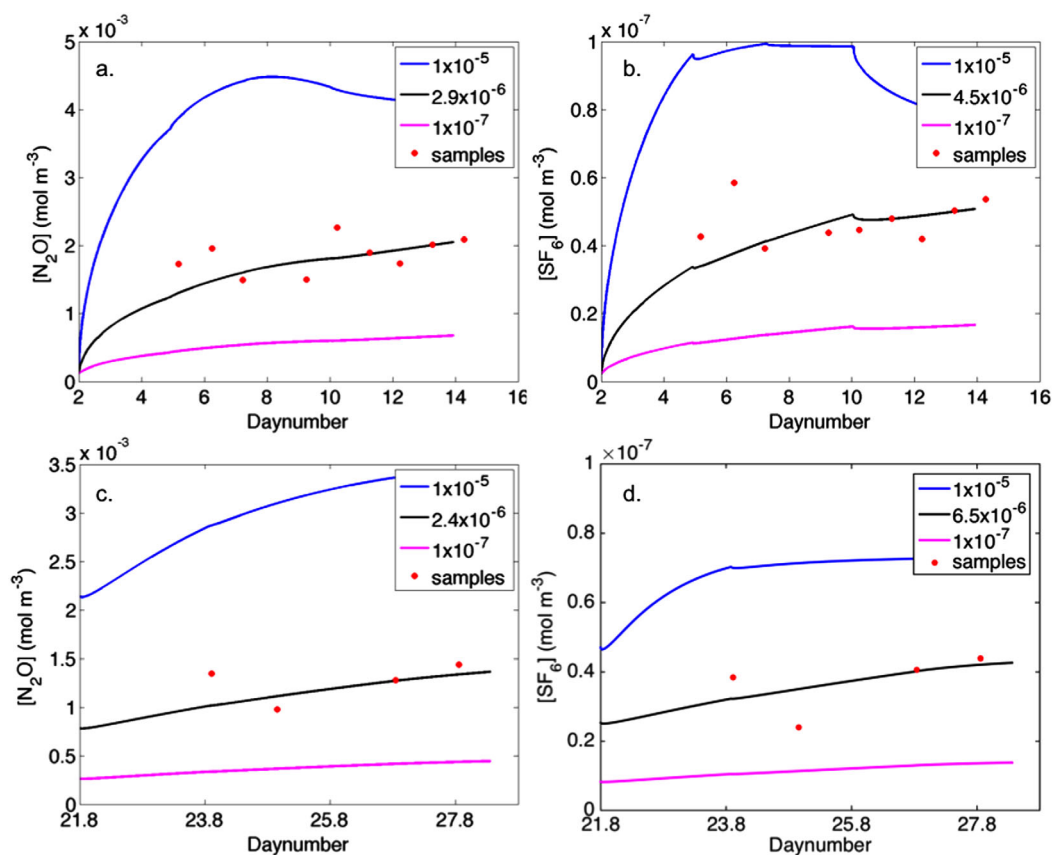
Figure 10. Model results for the diffusion coefficient (*D*) of N_2O and SF_6 into the ice for both (a, b) long lead and (c, d) short lead experiments. Red dots show the measured bulk concentration of the tracer in the ice. The smallest residual of error between the measured and modeled concentrations for both N_2O and SF_6 resulted from *D* values on the order of 10^{-6} cm^2 s^{-1} (black line). Blue and magenta lines represent the bulk gas concentration in the ice when for $D = 10^{-5}$ and 10^{-7} cm^2 s^{-1}, respectively. Inflections in the concentration are a result of changes in the ice-water boundary condition as tracer concentration in the water changed between scenarios.

sparingly soluble gases preferentially accumulated in gas-filled pores of sea ice and this can enhance the bulk gas diffusion, depending on the amount of gas-filled pore space. This solubility-driven behavior may be a direct consequence of bubble nucleation and buoyant vertical migration through sea ice brines, which have been observed in both field [*Zhou et al.*, 2013] and model studies [*Moreau et al.*, 2014]. It should also be noted that *Loose et al.* [2011] estimated much higher diffusion coefficients than those determined in this study. Comparing the magnitude of D_{O2} based on Graham's law and the estimate of D_{SF6} in this study, our value is 3 times smaller. The direct comparison of D_{SF6} estimated here (5.5×10^{-6}) and by *Loose et al.* [2011] (1.3×10^{-4}) differ by a factor of 23. These large differences may be a reflection of different experimental configuration or scale, which in turn lead to a difference in ice type. *Loose et al.* used a small tank, with a surface area of 0.19 m^2 (compared to the test basin surface area of 324 m^2), and this small tank was frozen over the entire surface. The salinity of the ice in *Loose et al.* [2011] was low, compared to the underlying saltwater, and this is likely an indication of more brine drainage and more gas-filled pore space. Consequently, these large differences in gas diffusivity might be interpreted as an experimental bias that leads to higher bubble content in the ice. Some authors have hypothesized that bubbles, trapped within sea ice brine channels can migrate vertically as a result of buoyancy [*Moreau et al.*, 2014], and *Zhou et al.* [2013] inferred that bubble migration may take place when the total porosity enters the range 0.075–0.1 The experiments by *Loose et al.* [2011] showed total porosity of 0.079 on average. However, that porosity is in fact lower than the porosity of 0.11 that is estimated for this experiment (see section 4.2). We have no easy explanation for this, except to propose that the gas-filled porosity may have been greater in the study by *Loose et al.* [2011].

The rate of molecular gas diffusion in water is in the range of 10^{-5} cm^2 s^{-1} [*Himmelblau*, 1964; *Jähne et al.*, 1987] and gas diffusion through freshwater ice is of the order of 10^{-7} cm^2 s^{-1} [*Ahn et al.*, 2008]. The sea ice

Table 2. Diffusion Coefficients, D, of the Gases Moving Through the Ice[a]

Scenario	D_{N2O}	D_{SF6}
0.09 open water (long lead experiment)	2.9×10^{-6}	4.5×10^{-6}
0.04 open water (Short lead experiment)	2.4×10^{-6}	6.5×10^{-6}
Average	2.65×10^{-6}	5.50×10^{-6}
Standard deviation	3.54×10^{-7}	1.41×10^{-6}

[a]N_2O and SF_6 values were determined using a finite difference model fit to measured bulk gas concentrations in the ice. All values of D are $cm^2\,s^{-1}$.

diffusivity measured in this experiment (e.g., $\sim10^{-6}$ $cm^2\,s^{-1}$) falls in between those two extremes, indicating that the porous nature of sea ice permits gas diffusion at a higher rate than in freshwater ice, but that the brine channel tortuosity and connectivity effectively restrict this rate to below what would be expected for a purely molecular process. Figure 8 depicts a vertical profile of the modeled N_2O concentration in the ice on Daynumber 30. Very little gas has diffused into the ice. These results, and the measured bulk ice concentration of 2×10^{-3} mol m^{-3} N_2O

and 4×10^{-8} mol m^{-3} SF_6 demonstrate that F_{ice} accounted for less than 2% of the total amount of tracer lost from the test basin through the experiment. The measured bulk concentration is comparable to a vertical average of the profile depicted in Figure 8. Thus, the amount of tracer incorporated into the ice was very small and no gas appeared to diffuse across the entire ice column and into the air. N_2O, unlike SF_6, has natural sources—possibly even within sea ice [*Rysgaard and Glud*, 2004], however, we have overwhelmed any natural production by large addition of N_2O to the system. At these concentrations, the ratio of gas to water partitioning or N_2O concentration in the brine is not relatable to studies of naturally occurring N_2O in sea ice [e.g., *Randall et al.*, 2012].

When the values of D are divided by the ice thickness (8.5 cm in the long lead experiment and 19 cm in short lead experiment), and corrected for a Schmidt number of 600, we obtain average values for k_{ice} of 8.92×10^{-4} and 4.93×10^{-4} m d^{-1}, respectively (Table 1). In comparison to the net air-sea gas exchange rate (k_{eff}), the median value of k_{ice} is 0.6% of the median k_{eff}. Hence, k_{ice} represents less than 1% of the total air-sea gas transfer rate. It is also worth noting that the ice in these experiments was warm, compared to what would be observed in the field for much of the year (Figure 7), with ice surface temperatures above $-5°C$ for much of the experiment.

The concentration of ^3He was not measured in the ice as we lacked the analytical capability to isolate ^3He from the ice so D_{3He} was approximated by taking the average of D_{SF6} and D_{N2O} estimate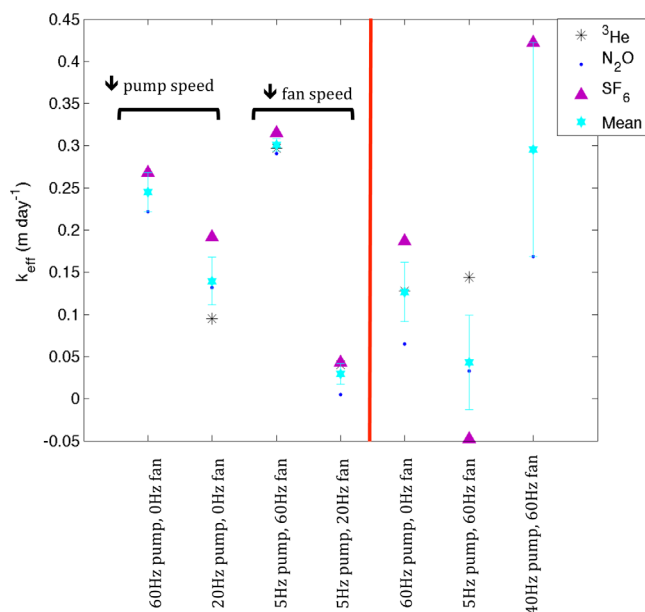s from the long and short lead experiments. The average was used because neither these results nor those of *Loose et al.* [2011] support a difference in bulk diffusivity that is dependent on molecular mass. After this correction is made to the ^3He measurements, Figure 11 shows that the k_{eff} values of ^3He are in line with those of N_2O and SF_6. If k_{eff} values from ^3He were much larger than for the other gases, we might suspect that D_{3He} is being underestimated, but this is not borne out in the results.

4.2. Neon and Helium-4 Gas Systematics
^4He and Ne were not purposefully introduced to the test basin. However, it is likely that they became supersaturated while bubbling air into the test basin to aid in mechanically agitating and dissolving the NaCl crystals, before the beginning of the experiment. However, the accumulation of these two

Figure 11. k_{eff} values for each forcing event, in order of scenario number. Error bars are the standard error of k_{eff} between the gases for each scenario. The red line separates 91% ice cover (to the left) from 96% ice cover (to the right).

inert gases in excess presents an opportunity to further explore gas systematics in the presence of sea ice. Before beginning that exploration, we attempt to clarify the terminology that will be used here: evasion refers to the transfer of gas from water to the air across the air-sea interface [*Peng et al.*, 1979]. The aqueous solubility refers to the amount of gas that the water can hold at equilibrium with the air [*Weiss*, 1971], and the diffusivity (D_{aq}) refers to the rate of molecular diffusion of the gas in water [*Asher and Wanninkhof*, 1998]. Solute rejection during ice growth describes the empirical observation that both gases and salts accumulate in the liquid phase during ice formation [*Killawee et al.*, 1998; *Tison et al.*, 2002; *Loose et al.*, 2009]. There is some debate whether this results from brine diffusion, brine expulsion, or from gravity drainage [*Cox and Weeks*, 1983; *Notz and Worster*, 2009]. Here we use the term solute rejection to emphasize gas accumulation in the water *during ice growth*. We use the term brine drainage to refer to flushing or gravity drainage that takes place after ice growth has stopped. Constant ice thickness is an important factor in these experiments as described in sections 2 and 3. Finally, we use the term "gas solubility in ice" to refer to the incorporation of gas molecules into the ice crystal structure [*Namiot and Bukhgalter*, 1965], similar to the clathrate structures that are observed at higher pressures.

Figure 6 shows the concentrations of ^{4}He and Ne over time in the test basin. At the beginning of the experiment, the concentration of ^{4}He exhibited 16% excess saturation and Ne exhibited 2% excess, indicating a strong thermodynamic tendency for ^{4}He to evade the water to the atmosphere. This evasion is reflected by the steady decreases in ^{4}He throughout the experiment (Figure 6). Ne, on the other hand, was only slightly supersaturated at the beginning of the lead experiments, meaning the tendency toward air-sea exchange was very weak. Contrary to the steady decreases in ^{4}He, the concentration of Ne initially increases during the long lead experiment and then decreases slightly or remains flat for the remainder of the short lead experiment. This distinct behavior between Ne and ^{4}He can be explained by the distinct aqueous solubilities and aqueous diffusivities of these two gases.

Because ^{4}He and Ne were already present in the test basin before freezing they were incorporated into the ice, just as salt would have been. As this brine drains into the tank, it will transport a certain quantity of Ne (and ^{4}He) back into the tank, explaining the gradual increase in Ne concentration. In the following discussion, we will first describe how brine drainage affects Ne and He, and then discuss how ice formation affects He and Ne differently, and finally we will describe how gas exchange affected He (and Ne to a lesser degree). We can use the change in salinity in the tank below the ice to infer the partitioning of salt (and gases) between the water and the ice. This can be used to estimate solute rejection during ice growth, brine drainage when ice thickness is stable, and ice melt. We can only estimate one term at a time, so we have to assume that one term is dominating the net change in the salinity of the test basin. As described above, we can separate solute rejection and brine drainage, based upon whether ice thickness is growing or is stable. The time frame of melting is less clear, but we can use the air and ice temperature as diagnostics for when melt can occur (Figure 7).

The progressive increase of Ne in the tank water during the short and long lead experiments when ice thickness was constant indicates that Ne is building up in the test basin through brine drainage. To constrain brine drainage, we use the salt balance in the test basin. Using the equations of Cox and Weeks [1983], and average values for ice temperature ($-2°$C), and bulk ice salinity (S_i) of 6.5 psu, we estimate that the ice porosity (ϕ) is 0.11, and the brine salinity (S_{br}) is 59 psu, where $S_{br} = S_i/\phi$. Using S_{br}, and the observed change in salinity in the tank (Figure 2), we estimate that about 1.55 m^3 of brine drained from the ice between day 0 and day 15. If we make the assumption that Ne, ^{4}He, and salt are incorporated into the brine equivalently (i.e., $S_{br}/S_w = [C_{br}]/[C_w]$ [*Loose et al.*, 2009]), brine drainage can account for approximately 66% of the increase in the Ne concentration that was observed from day 0 to day 15. $[C_{br}]$ and $[C_w]$ are the concentrations in the brine and in the water, respectively. Tighter constraint on gas transport with brine drainage is difficult to achieve; there are very few measurements of any gas in sea ice brines as it is a difficult measurement to make, but the salt budget demonstrates that brine drainage is of the right magnitude to explain the accumulation of Ne in the test basin.

4.2.1. Inclusion of ^{3}He, ^{4}He Not Ne in the Ice Crystal Lattice

The increase in Ne concentration from days 15 to 23, during a period of active ice growth (Figure 6) can be attributed to solute rejection of Ne during ice formation. During this transition period from the long lead to the short lead, an additional 10 cm of ice was grown over the entire tank surface (foam insulation was installed to mitigate freezing over the surface of the short lead.) During the freezing event for the short

lead, the salinity in the tank increased by 0.96 psu. By mass, this indicates that 78% of the salt was rejected from the ice during freezing, consistent with predictions [*Cox and Weeks*, 1983] (section S2 of the supporting information contains a complete derivation of this calculation). Concurrently, Ne concentration in the test basin increased from 8.90 to 8.95 μmol m^{-3} (days 15–22, Figure 6). The increase in concentration indicates that Ne was excluded from the ice crystal lattice. Whether Ne is preferentially excluded or included in ice has been a topic of debate [*Hood et al.*, 1998]. By analogy with aqueous solubility, the process is referred to as gas solubility in ice, and is defined as K=C_{ice}/C_w, where C_{ice} is the equilibrium gas concentration in the ice and C_w is the equilibrium concentration in water [*Killawee et al.*, 1998]. The two available literature values are K_{Ne}=1.4 and K_{Ne}=0.9, with the first value indicating that Ne is preferentially incorporated into the ice [*Hood et al.*, 1998, and references therein]. We can infer C_{ice} from the increase in Ne concentration within the test basin and the water concentration before the additional 10 cm of ice were formed. This calculation results in C_{ice}/C_{water}=7.53$\times$10^{-6}/9.08$\times$10^{-6} or K_{Ne}=0.85. These data support the latter value of K_{Ne}=0.9. We can neglect loss of Ne to air-water gas exchange because the entire tank surface is covered by ice or by insulating foam.

The 10 cm of ice formation before the short lead experiment had the opposite effect on both the ^{3}He and ^{4}He concentrations; their concentrations were both lower after freezing, indicating they were preferentially included in the ice crystal lattice. If we estimate K_{He} in the same manner as described above for K_{Ne}, the ^{4}He concentrations indicate that K_{He}=1.5, which is not far from the literature estimate for K_{He} = 1.9 [*Hood et al.*, 1998]. The same calculation for ^{3}He yields K_{He}=4.3, which is more difficult to explain. This could be an isotopic effect, which has been observed during air-sea gas exchange—another solubility-controlled process [*Tempest and Emerson*, 2013]. In that study, the authors observed that the ratio of heavy:light isotopes dissolved in water, divided by the ratio in the gas phase was 0.996 for Ar and 0.993 for Ne. If we compute the same heavy:light ratio in ice divided by the heavy:light ratio in water, we get an ice:water fractionation ratio of 0.48, implying much stronger kinetic fractionation. However, the air-water gradient in ^{3}He was orders of magnitude greater than for ^{4}He, indicating that any air-sea exchange pathway would have affected ^{3}He much more than ^{4}He or Ne. Collectively, these results do confirm previous research indicating there is a critical size threshold beyond which a molecule does not fit within the 1-H structure of ice formed at atmospheric pressure [*Namiot and Bukhgalter*, 1965]. He is smaller than the threshold and is consequently favored for incorporation in the ice; Ne is slightly too large and not favored for incorporation.

4.3. Gas Budget Corrections for Melting and Brine Drainage

As described in section 4.2.1, there are important differences in the molecular properties of gases that affect their partitioning in sea ice covered waters. These differences, including differences in aqueous solubility and aqueous diffusivity, can also explain how ^{4}He decreased continually throughout the lead experiments while Ne first increased and then remained relatively stable. To reiterate, ^{4}He exceeded saturation by 16% at the onset of the experiment, and decreased to 5% excess saturation by the end of the experiment. Ne was less than 2% excess saturated, and increased to 4% by the end of the experiment. Consequently, the air-sea concentration gradients favored ^{4}He gas exchange more than Ne. This, and the twofold greater aqueous diffusivity between He (4.2 $\times$ 10^{-6} cm^2 s^{-1}) and Ne (2.4 $\times$ 10^{-6} cm^2 s^{-1}), leads to a larger helium gas flux. Both gases would also have been transported from the ice to the tank by brine drainage, but air-sea exchange of ^{4}He was greater, producing a net loss that masked the brine drainage effect. By the end of the experiment, after day 20, Ne can be observed to decrease, and this is likely due to gas exchange and ice melt as Ne was in greater excess and the air temperature was warm during this period and the salinity in the tank decreased (Figure 2).

Having observed how Ne and ^{4}He were affected by brine drainage and ice melt processes, a salt balance correction was applied to N_2O, SF_6, and ^{3}He before computing the gas transfer velocity. For N_2O and SF_6, the bulk ice concentrations were used to correct for brine drainage and ice melt. The bulk concentration in the ice for ^{3}He was calculated using the bulk diffusivity, calculated in section 4.1. These corrections had minimal effect on the gas transfer velocity, as the total gas transport by brine drainage was small compared to air-sea exchange.

Overall, the effect of gas diffusion into the ice and brine drainage from the ice impacted the gas budgets in the tank by less than 2–3%. The largest effect on gas budgets (aside from air-sea gas exchange) is solute rejection during freezing. In this experiment, 19 cm was formed above a tank with an effective depth of

2.2 m (Vol/surface area), which could lead to ~6% increase in the gas concentration. However, the need to correct for this effect was avoided by adding the gas to the water after ice formation.

4.4. The Physical Processes Affecting the Gas Transfer Velocity, k_{eff}

As stated in section 1, the principal objective of the GAPS experiment was to observe the rate of air-sea gas exchange under a range of plausible forcing conditions in the ice zone. Here we briefly describe the overall tendencies observed in k_{eff} during the lead experiments. However, we leave the bulk of this interpretation to a forthcoming manuscript that will examine and validate the forcing conditions throughout the experiment and relate those to the observed magnitudes of k.

We observed measurable increases in the gas flux and in k_{eff} when the water current speed and/or the wind tunnel speed increased. As expected, k_{eff} was also greater, when ice cover was reduced (Figure 11 and Table 1). Research in the past has shown that k_{eff} increases with wind speed and the amount of open water, but here it is apparent that velocity shear, produced by the velocity differential between ice and water, plays an important role in ice-covered areas as well. These water currents can lead to surface turbulence and surface renewal of gases [*Loose et al.*, 2009].

There are some interesting details and a few inconsistencies between successive forcing events that merit further discussion. For example, during two forcing events with low current speed: Scenario 4: 5 Hz pump and 20 Hz fan and Scenario 6: 5 Hz pumps and 60 Hz fan, we observed very low gas transfer velocity: $k_{eff} = 0.03$ and 0.00 m/d, respectively. In comparison, when the pumps are circulating at or above 20 Hz, there is a significant increase in gas exchange (see e.g., Figure 11 and Table 1). These results seem to indicate that wind alone (in the range of U_{10} from 0 to 7 m/s) over restricted fetch has minimal impact on gas flux. However, there may be another important explanation for low k_{eff} at the higher wind speed: gas exchange in the lead will tend to deplete the surface water, leading to a diminished air-water concentration gradient. If this water is not replaced by adjacent gas-rich water, the air-water concentration differential will be reduced and the estimate of k will decline. This may have been the case in Scenarios 4 and 6 where the water velocity was very low (<2 cm/s). In another scenario (Scenario 3), high wind and greater fetch yielded stronger water current speeds (see water velocity in Table 1). This current can replenish the water in the lead and permit a higher rate of gas exchange—a result that is borne out in the higher value of k for Scenario 3 ($k_{eff} = 0.33$ m d^{-1}). In this way, it is clear that the combination of wind and currents in the sea ice zone may be more critical than in any other physical system that has been studied to this point. As *Zappa et al.* [2007] have pointed out, the addition of wind to an ambient water current eventually saturates the turbulent kinetic energy production, and additional current has almost negligible impact on the rate of gas exchange. That same saturation may not occur as quickly in the sea ice zone, as the divergence between ice and water is necessary to replenish openings with new gas-rich water. In the real sea ice zone, wind and currents almost always lead to ice-water divergence, so this process is almost implicit. It therefore may be an artifact of this experiment that the ice—adhered to the walls—does not move when the wind blows, leading to low rates of water replenishment at low current speeds.

This mechanism can be extended to show how the transfer velocity increases dramatically when both the pumps and the fan are operating on high (Scenario 7 and Figure 11 and Table 1). Under these conditions, we observed the highest rate of k_{eff}, indicating that the combination of wind and water currents may be additive in their effect on gas exchange.

4.5. Uncertainty in Estimates of k_{eff}

Having corrected the dissolved gas budgets for both brine drainage and ice melt, as described in section 4.3, and for F_{ice}, as detailed in section 2.3, and having accounted for Schmidt number effects, it is apparent that some disagreement still exists between the estimates of k_{eff} between the conserved gases (SF_6, N_2O, and ^{3}He). These differences reflect uncertainty in the analytical methods for each gas, including uncertainty in the calibration, and anomalous effects such as small changes in ice melt or formation that are difficult to quantify. To formally establish the level of uncertainty in the estimates of k_{eff}, we propagated the analytical and model uncertainty through equations (1–10), which are used to calculate individual values of k_{eff} for each gas. It was only possible to carry out this analysis for N_2O and SF_6 as these were the two gases measured in the ice. We have assumed that the uncertainty for ^{3}He, ^{4}He, and Ne will be less as they have a smaller analytical uncertainty. The method for this error analysis is described in the supporting information.

Table 3. Percent Error of the k_{eff} Values for Each Tracer Gas During Each Scenario Calculated Using the Rules of Error Propagation and Found Empirically as the Standard Error Between the k_{eff} Calculated for Each Tracer During Each Scenario

Scenario	N_2O Uncertainty (%)	SF_6 Uncertainty (%)	Empirical Uncertainty Between Gases (%)
1	40.6	34.1	10.5
2	52.5	35.5	21.3
3	36.6	34.7	2.54
4	171.9	102.3	235
5	19.0	17.8	54.2
6	36.5	20.3	168
7	22.7	20.5	75.4
Avg	38.6	34.1	81.0

Based on this analysis, the uncertainty in k_{eff} for N_2O and SF_6 was of similar range, varying between 18 and 53%, with the exception of Scenario 4 for which the uncertainty in k_{eff} from N_2O was 173% and SF_6 was 102% (Table 3). As a second method of comparison, we can calculate the variability in the estimates of k_{eff} from SF_6, N_2O, and ^3He—once corrected for the Schmidt number effects, these estimates of k_{eff} should be identical. The variability between k_{eff} from individual gases ranged between 10.5 and 235% where Scenario 4 again showed the greatest variability (Table 3). On average, the empirical variability between gases was greater than the values from the uncertainty analysis from supporting information. This may indicate that there are other sources of variability not accounted for in our uncertainty analysis. Possible other sources of variability include sporadic frazil ice formation and melt. Frazil ice formation complicates air-sea exchange by several mechanisms and was a recurring process during Scenarios 4 and 6 (Table 1), as the water current was low at these times and the wind blew cold air across the water surface causing it to quickly freeze. Melt occurred during Scenarios 5 and 7 as the air temperature was increased to reduce the formation of frazil ice.

Another factor that may have resulted in some error is the circulation pattern of the test basin at CRREL. At one end of the test basin, there are multiple pipes that connect to a 61.6 m^3 fully enclosed tank. No water was pumped between the tanks, but a pressure gradient resulting from the pressure of the water current pumps as well as diffusion likely resulted in some exchange and dilution of the tracers in the test basin. A pressure differential would only form during a major change in the water currents of the main tank and would quickly equilibrate. Therefore, this likely did not result in a great deal of transfer between the tanks. N_2O and SF_6 were in the tank for a month before ^3He was added allowing their concentrations more time to equilibrate between the test basin and the additional tank. Thus, their concentrations are likely higher in the enclosed tank and the ^3He data would be more affected by dilution from this tank than the other two gases.

Given that the standard error between gases exceeded the error from the uncertainty analysis, we opted to use the standard error to establish the level of significance of our estimates of k_{eff} during each of the scenarios with unique gas exchange forcing conditions. The error bars in Figure 11 reflect this significance level, and it is apparent that despite large uncertainties associated with some of the values of k_{eff}, the GAPS experiment was able to resolve statistically significant differences in the gas transfer velocity.

5. Summary

In these experiments, we have determined a mean rate of N_2O diffusivity in saltwater ice of 2.65×10^{-6} cm^2 s^{-1} and a mean rate of SF_6 diffusivity of 5.50×10^{-6} cm^2 s^{-1} indicating that the lower solubility gas (SF_6) experienced faster diffusion, possibly as a result of gas-liquid partitioning in the porous microstructure. The total diffusive gas flux into the ice was less than 2% of total water column gas losses. Much of this gas remained stored in the ice microstructure itself. A similar result has been reported by an earlier laboratory experiment [*Loose et al.*, 2011], although here we report values of k_{ice} that are significantly smaller than the previous ones. However, both studies indicate that ventilation of the water column via diffusion through first year ice is a slow process.

The unexpected excess saturation of ^4He and Ne yielded further opportunity to study the processes affecting gas budgets in the sea ice zone. The behavior of both gases was predictable, based upon our understanding of gas processes in the ice zone; ^4He tended to evade the tank in a fashion similar to SF_6, N_2O, and ^3He. However, Ne was not excessively saturated in the test basin and consequently, its concentration increased through the process of brine drainage with minimal offset by air-sea gas exchange. As a rough scaling to the real sea ice zone, we estimate that approximately 8% of the tank volume became sea ice. This

is equivalent to an ice layer of 2.4 m above a 30 m water column. Under these circumstances, brine drainage and gas diffusion into the ice altered the gas budget by 2–3%, and these processes tended to largely offset each other.

This leaves interfacial air-sea exchange through partial ice cover as the main air-sea transport mechanism. The GAPS experiment found that, in the presence of sea ice, the magnitude of k_{eff} is significantly influenced not only by the fraction of open water but also by wind speed and water current speed. An escalation of any of these factors results in a significant increase in the rate of gas exchange.

References

Ahn, J., M. Headly, M. Wahlen, E. J. Brook, P. A. Mayewski, and K. C. Taylor (2008), CO_2 diffusion in polar ice: Observations from naturally formed CO_2 spikes in the Siple Dome (Antarctica) ice core, *J. Glaciol.*, *54*(187), 685–695, doi:10.3189/002214308786570764.

Arrigo, K. R., and G. L. van Dijken (2007), Interannual variation in air-sea CO_2 flux in the Ross Sea, Antarctica: A model analysis, *J. Geophys. Res.*, *112*, C03020, doi:10.1029/2006JC003492.

Asher, W., and R. Wanninkhof (1998), Transient tracers and air-sea gas transfer, *J. Geophys. Res.*, *103*(C8), 15,939–15,958.

Bullister, J., D. P. Wisegarver, and F. A. Menzia (2002), The solubility of sulfur hexafluoride in water and seawater, *Deep Sea Res., Part I*, *49*, 175–187.

Cox, G. F. N., and W. F. Weeks (1983), Equations for determining the gas and brine volumes in sea ice samples, *J. Glaciol.*, *29*(102), 306–316.

Crabeck, O., B. Delille, S. Rysgaard, D. N. Thomas, N.-X. Geilfus, B. Else, and J.-L. Tison (2014), First "in situ" determination of gas transport coefficients (D_{O_2}, D_{Ar}, and D_{N_2}) from bulk gas concentration measurements (O_2, N_2, Ar) in natural sea ice, *J. Geophys. Res. Oceans*, *119*, 6655–6668, doi:10.1002/2014JC009849.

Delille, B., et al. (2014), Southern Ocean CO_2 sink: The contribution of the sea ice, *J. Geophys. Res. Oceans*, *119*, 6340–6355, doi:10.1002/2014JC009941.

Fanning, K. A., and L. M. Torres (1991), ^{222}Rn and ^{226}Ra: Indicators of sea-ice effects on air-sea gas exchange, *Polar Res.*, *10*(1), 51–58, doi:10.3402/polar.v10i1.6727.

Golden, K. M. (2001), Brine percolation and the transport properties of sea ice, *Ann. Glaciol.*, *33*(1), 28–36, doi:10.3189/172756401781818329.

Golden, K. M., S. F. Ackley, and V. I. Lytle (1998), The percolation phase transition in sea ice, *Science*, *282*, 2238–2241.

Gosink, T. A., J. G. Pearson, and J. J. Kelley (1976), Gas movement through sea ice, *Nature*, *263*(5572), 41–42, doi:10.1038/263041a0.

Hain, M. P., D. M. Sigman, and G. H. Haug (2010), Carbon dioxide effects of Antarctic stratification, North Atlantic Intermediate Water formation, and subantarctic nutrient drawdown during the last ice age: Diagnosis and synthesis in a geochemical box model, *Global Biogeochem. Cycles*, *24*, GB4023, doi:10.1029/2010GB003790.

Himmelblau, D. M. (1964), Diffusion of dissolved gases in liquids, *Chem. Rev.*, *64*(5), 527–550, doi:10.1021/cr60231a002.

Ho, D. T., C. L. Sabine, D. Hebert, D. S. Ullman, R. Wanninkhof, R. C. Hamme, P. G. Strutton, B. Hales, J. B. Edson, and B. R. Hargreaves (2011), Southern Ocean gas exchange experiment: Setting the stage, *J. Geophys. Res.*, *116*, C00F08, doi:10.1029/2010JC006852.

Hood, E. M., B. L. Howes, and W. J. Jenkins (1998), Dissolved gas dynamics in perennially ice-covered Lake Fryxell, Antarctica, *Limnol. Oceanogr.*, *43*(2), 265–272.

Jähne, B., G. Heinz, and W. Dietrich (1987), Measurement of the diffusion coefficients of sparingly soluble gases in water, *J. Geophys. Res.*, *92*(C10), 10,767–10,776, doi:10.1029/JC092iC10p10767.

Killawee, J. A., I. J. Fairchild, J.-L. Tison, L. Janssens, and R. Lorrain (1998), Segregation of solutes and gases in experimental freezing of dilute solutions: Implications for natural glacial systems, *Geochim. Cosmochim. Acta*, *62*, 3637–3655.

Loose, B., and P. Schlosser (2011), Sea ice and its effect on CO_2 flux between the atmosphere and the Southern Ocean interior, *J. Geophys. Res.*, *116*, C11019, doi:10.1029/2010JC006509.

Loose, B., W. R. McGillis, P. Schlosser, D. Perovich, and T. Takahashi (2009), Effects of freezing, growth, and ice cover on gas transport processes in laboratory seawater experiments, *Geophys. Res. Lett.*, *36*, L05603, doi:10.1029/2008GL036318.

Loose, B., P. Schlosser, D. Perovich, D. Ringelberg, D. T. Ho, T. Takahashi, J. Richter-Menge, C. M. Reynolds, W. R. Mcgillis, and J.-L. Tison (2011), Gas diffusion through columnar laboratory sea ice: Implications for mixed-layer ventilation of CO2 in the seasonal ice zone, *Tellus, Ser. B*, *63*(1), 23–39, doi:10.1111/j.1600-0889.2010.00506.x.

Loose, B., W. R. McGillis, D. Perovich, C. J. Zappa, and P. Schlosser (2014), A parameter model of gas exchange for the seasonal sea ice zone, *Ocean Sci.*, *10*(1), 17–28, doi:10.5194/os-10-17-2014.

McPhee, M. G. (1992), Turbulent heat flux in the upper ocean under sea ice, *J. Geophys. Res.*, *97*(C4), 5365–5379, doi:10.1029/92JC00239.

Mesarchaki, E., C. Krauter, K. E. Krall, M. Bopp, F. Heilleis, J. Williams, and B. Jahne (2014), Measuring air-sea gas exchange velocities in a large scale annular wind-wave tank, *Ocean Sci.*, *11*, 1643–1689.

Moreau, S., M. Vancoppenolle, J. Zhou, J.-L. Tison, B. Delille, and H. Goosse (2014), Modelling argon dynamics in first-year sea ice, *Ocean Model.*, *73*, 1–18, doi:10.1016/j.ocemod.2013.10.004.

Namiot, A. Y., and E. B. Bukhgalter (1965), Clathrates formed by gases in ice, *J. Struct. Chem.*, *6*, 873–874.

Notz, D., and M. G. Worster (2009), Desalination processes of sea ice revisited, *J. Geophys. Res.*, *114*, C05006, doi:10.1029/2008JC004885.

Peng, T.-H., W. S. Broecker, G. G. Mathieu, and Y.-H. Li (1979), Radon evasion rates in the Atlantic and Pacific oceans as determined during the Geosecs program, *J. Geophys. Res.*, *84*(C5), 2471–2486.

Petrich, C., and H. Eicken (2009), Growth, structure and properties of sea ice, in *Sea Ice*, edited by D. N. Thomas and G. S. Dieckmann, pp. 23–77, Wiley-Blackwell, Oxford, U. K.

Randall, K., M. Scarratt, M. Levasseur, S. Michaud, H. Xie, and M. Gosselin (2012), First measurements of nitrous oxide in Arctic sea ice, *J. Geophys. Res.*, *117*, C00G15, doi:10.1029/2011JC007340.

Rutgers van der Loeff, M. M., N. Cassar, M. Nicolaus, B. Rabe, and I. Stimac (2014), The influence of sea ice cover on air-sea gas exchange estimated with radon-222 profiles, *J. Geophys. Res. Oceans*, *119*, 2735–2751, doi:10.1002/2013JC009321.

Rysgaard, S., and R. N. Glud (2004), Anaerobic N_2 production in Arctic sea ice, *Limnol. Oceanogr.*, *49*(1), 86–94, doi:10.4319/lo.2004.49.1.0086.

Rysgaard, S., R. N. Glud, M. K. Sejr, J. Bendtsen, and P. B. Christensen (2007), Inorganic carbon transport during sea ice growth and decay: A carbon pump in polar seas, *J. Geophys. Res.*, *112*, C03016, doi:10.1029/2006JC003572.

Stephens, B. B., and R. F. Keeling (2000), The influence of Antarctic sea ice on glacial–interglacial CO_2 variations, *Nature*, *404*(6774), 171–174, doi:10.1038/35004556.

Takahashi, T., et al. (2009), Climatological mean and decadal change in surface ocean pCO_2, and net sea–air CO_2 flux over the global oceans, *Deep Sea Res., Part II*, *56*(8–10), 554–577, doi:10.1016/j.dsr2.2008.12.009.

Tamura, T., K. Ohshima, and S. Nihashi (2008), Mapping of sea ice production for Antarctic coastal polynyas, *Geophys. Res. Lett.*, *35*, L07606, doi:10.1029/2007GL032903.

Tempest, K. E., and S. Emerson (2013), Kinetic isotopic fractionation of argon and neon during air–water gas transfer, *Mar. Chem.*, *153*(0), 39–47, doi:10.1016/j.marchem.2013.04.002.

Tison, J.-L., C. Haas, M. M. Gowing, S. Sleewaegen, and A. Bernard (2002), Tank study of physico-chemical controls on gas content and composition during growth of young sea ice, *J. Glaciol.*, *48*, 177–191.

Wanninkhof, R. (1992), Relationship between wind speed and gas exchange over the ocean, *J. Geophys. Res.*, *97*(C5), 7373–7382, doi:10.1029/92JC00188.

Wanninkhof, R., J. R. Ledwell, W. S. Broecker, and M. Hamilton (1987), Gas exchange on Mono Lake and Crowley Lake, California, *J. Geophys. Res.*, *92*(C13), 14,567–14,580, doi:10.1029/JC092iC13p14567.

Weiss, R. F. (1971), Solubility of helium and neon in water and seawater, *J. Chem. Eng. Data*, *16*(2), 235–241, doi:10.1021/je60049a019.

Weiss, R. F. (1974), Carbon dioxide in water and seawater: The solubility of a non-ideal gas, *Mar. Chem.*, *2*, 203–215, doi:10.1016/0304-4203(74)90015-2.

Weiss, R. F., and B. A. Price (1980), Nitrous oxide solubility in water and seawater, *Mar. Chem.*, *8*(4), 347–359, doi:10.1016/0304-4203(80)90024-9.

Zappa, C. J., W. R. McGillis, P. A. Raymond, J. B. Edson, E. J. Hintsa, H. J. Zemmelink, J. W. H. Dacey, and D. T. Ho (2007), Environmental turbulent mixing controls on air-water gas exchange in marine and aquatic systems, *Geophys. Res. Lett.*, *34*, L10601, doi:10.1029/2006GL028790.

Zhou, J., B. Delille, H. Eicken, M. Vancoppenolle, F. Brabant, G. Carnat, N.-X. Geilfus, T. Papakyriakou, B. Heinesch, and J.-L. Tison (2013), Physical and biogeochemical properties in landfast sea ice (Barrow, Alaska): Insights on brine and gas dynamics across seasons, *J. Geophys. Res. Oceans*, *118*, 3172–3189, doi:10.1002/jgrc.20232.